

Nanocrystalline structure of nanobump generated by localized photoexcitation of metal film

Dmitriy S. Ivanov,^{1,2,3} Zhibin Lin,^{1,4} Baerbel Rethfeld,³ Gerard M. O'Connor,² Thomas J. Glynn,² and Leonid V. Zhigilei^{1,a)}

¹*Department of Materials Science and Engineering, University of Virginia, Charlottesville, Virginia, USA*

²*National Centre for Laser Applications, National University of Ireland, Galway, Ireland*

³*Department of Physics and Optimas Research Center, Technical University of Kaiserslautern, Kaiserslautern, Germany*

⁴*Department of Physics, Renewable Energy Materials Research Science and Engineering Center (REMRSEC), Colorado School of Mines, Golden, Colorado, USA*

(Received 16 October 2009; accepted 25 November 2009; published online 14 January 2010)

The extreme cooling rates in material processing can be achieved in a number of current and emerging femtosecond laser techniques capable of highly localized energy deposition. The mechanisms of rapid solidification of a nanoscale region of a metal film transiently melted by a localized photoexcitation are investigated in a large-scale atomistic simulation. The small size of the melted region, steep temperature gradients, and fast two-dimensional electron heat conduction result in the cooling rate exceeding 10^{13} K/s and create conditions for deep undercooling of the melt. The velocity of the liquid/crystal interface rises up to the maximum value of ~ 80 m/s during the initial stage of the cooling process and stays approximately constant as the temperature of the melted region continues to decrease. When the temperature drops down to the level of $\sim 0.6T_m$, a massive homogeneous nucleation of the crystal phase inside the undercooled liquid region takes place and prevents the undercooled liquid from reaching the glass transition temperature. The prediction of the nanocrystalline structure of the surface features generated in laser nanoprocessing has implications for practical applications of nanostructured surfaces and calls for experimental verification of the computational results. © 2010 American Institute of Physics. [doi:10.1063/1.3276161]

I. INTRODUCTION

The kinetics and mechanisms of rapid solidification of pure metals under conditions of strong undercooling have been the subjects of active experimental exploration and theoretical analysis. Two general approaches are used for achieving the conditions of strong undercooling in liquid metals. The first approach is based on the elimination of the nucleation sites for heterogeneous nucleation of the solid phase. It can be traced back to the experiments on small metal droplets by Turnbull and Cech,¹ where an undercooling by as much as $\sim 18\%$ below the equilibrium melting temperature has been observed before the onset of rapid solidification. An alternative way to create a strong undercooling is to rapidly quench melted metal with a cooling rate that is sufficiently high to kinetically inhibit the solidification process. Various methods of quenching have been developed and applied for fabrication of materials with fine grain structures, nonequilibrium crystalline and (in the case of metallic alloys) amorphous phases.²

Irradiation of metal targets by short (picosecond and femtosecond) laser pulses provides an attractive alternative to conventional quenching techniques (such as the melt spinning or splat cooling). The shallow depths of the laser energy deposition and steep temperature gradients, typically produced by the short pulse laser irradiation, combined with the high thermal conductivity of metals can lead to the record

cooling rates of more than 10^{12} K/s.^{3,4} Strong undercooling and rapid resolidification occurring under such conditions may result in the formation of the metastable structures and phases that cannot be produced with other methods. In particular, metallic glass formation for systems not previously considered being glass formers has been demonstrated in nanosecond- and picosecond-pulse laser quenching.^{3,5-7} While the existence of pure one-component amorphous metals is not prohibited by theory,^{2,8} they have not been produced by conventional cooling methods (a notable exception is a high-pressure metallic glass produced by rapid cooling of liquid Ge at high, above 7 GPa, pressure⁹). There have been recent reports suggesting that an amorphous layer could be generated at the bottom of the ablation crater in laser ablation of Au and Cu targets.^{10,11} These experiments were performed in air and the reduction of x-ray diffraction peaks, used in this work as the evidence of the formation of a stable layer of amorphous metal, is likely to have alternative explanations. Nevertheless, with the extremely high cooling rates achievable in the short pulse laser quenching, it is not unreasonable to explore if the conditions for amorphization of a pure metal can be realized.

The maximum cooling rates in laser-material interactions can be achieved when the laser energy deposition is confined not only within the thin surface layer of the irradiated target but also in the lateral dimensions, creating conditions for even faster two-dimensional (for thin films) or three-dimensional (for bulk targets) heat transfer from the absorption region. The localized laser energy deposition can

^{a)}Electronic mail: lz2n@virginia.edu.

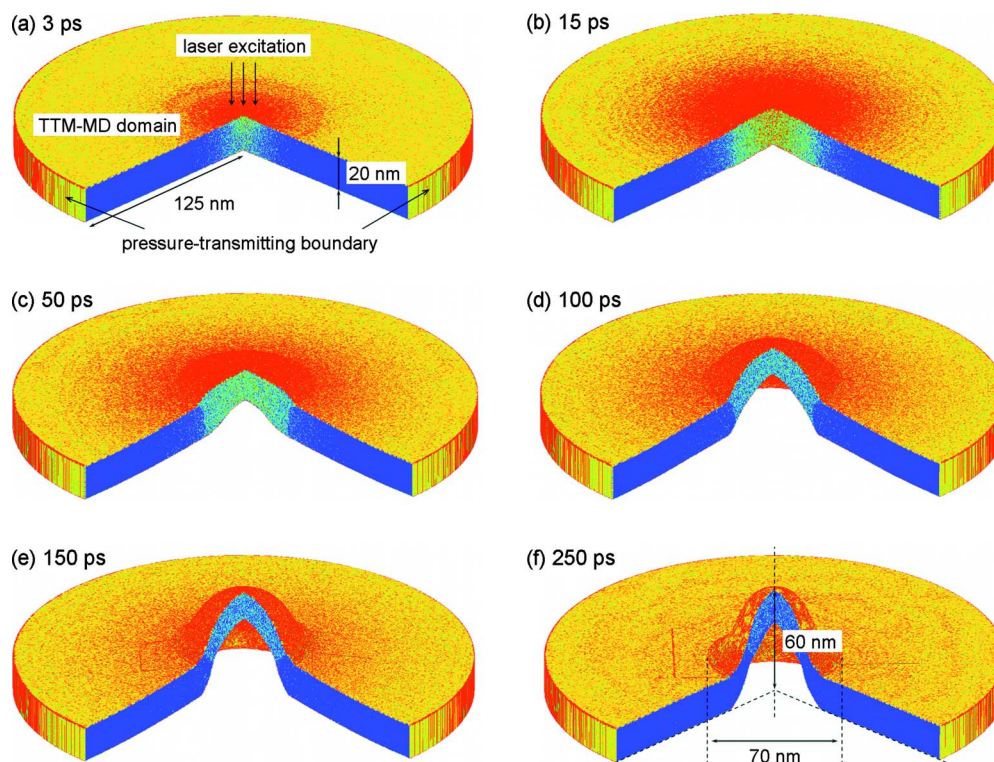


FIG. 1. (Color online) Snapshots from a simulation of the generation of a nanobump on a 20 nm Ni film located on a transparent substrate and subjected to a localized excitation by a 200 fs laser pulse. The size of the region of the optical excitation is 10 nm. The snapshots show the MD part of the combined atomistic-continuum model, with pressure-transmitting boundary conditions applied circumferentially around the MD circular slab and continuum equations for the lattice and electron temperatures solved in a wide region extending more than 300 nm from the center of the computational domain. Atoms are colored according to their potential energy, from blue color corresponding to a low potential energy of -4.2 eV to red color corresponding to a high potential energy of -3.6 eV (the cohesive energy of the EAM Ni fcc crystal is 4.45 eV). A sector of the film is blanked to show the distribution of the potential energy inside the film.

be achieved by using tightly focused laser beams^{12–15} or taking advantage of the local field enhancement in the vicinity of a tip of a scanning probe microscope^{16–20} or a deposited nano/microparticle.^{21,22} Analysis of the microstructure of the small regions experiencing localized melting and resolidification can provide insights into the relative contribution of competing resolidification mechanisms, which may include epitaxial regrowth of the self-substrate, nucleation of crystallites throughout the undercooled melted region, and the formation of an amorphous structure. The small size of the laser-modified zone, however, makes the experimental characterization of the microstructure difficult. In this paper, we use the results of a large-scale atomistic simulation of laser-induced generation of a nanoscale surface topographic feature (nanobump) to perform a detailed computational analysis of the resolidification process occurring under conditions of localized laser energy deposition. The physical insights into the mechanisms defining the microstructure of the resolidified region, revealed in the simulation, are likely to stimulate experimental investigations in this area.

II. COMPUTATIONAL MODEL

The melting and resolidification processes are investigated in this work based on the results of a large-scale atomistic simulation of a metal film subjected to a highly localized laser excitation.²³ The simulation is performed with a combined atomistic-continuum model^{24,25} that couples the

classical molecular dynamics (MD) method with a continuum-level description of the laser excitation and subsequent relaxation of the conduction band electrons. The model accounts for the fast electron heat conduction in the metal film and provides an adequate representation of the fast heating and cooling of the region of the laser energy deposition. A complete description of the combined atomistic-continuum model is given in Ref. 24, whereas the computational setup used in the simulation is described in Ref. 23. Briefly, the simulation is performed for a 20 nm Ni film deposited on a transparent substrate. The MD part of the computational system consists of $\sim 85\,000\,000$ atoms and has a shape of a circular slab with diameter of 250 nm [Fig. 1(a)]. The coupled electron and lattice heat conduction equations are solved in a larger region extending more than 300 nm from the center of the system in the radial (parallel to the surface of the film) direction. The interatomic interactions in the MD part of the system are described by the embedded-atom method (EAM) potential in the form suggested in Ref. 26. The interaction of Ni atoms with the substrate is described by the Lennard-Jones potential with parameters chosen to represent an adhesion of the Ni film to the substrate, which is assumed to be ten times weaker than the effective strength of Ni–Ni interaction. The values of the electron and lattice heat capacity, thermal conductivity, and electron-phonon coupling factor are given in Refs. 24 and 25. The energy deposition from a 200 fs laser pulse is localized

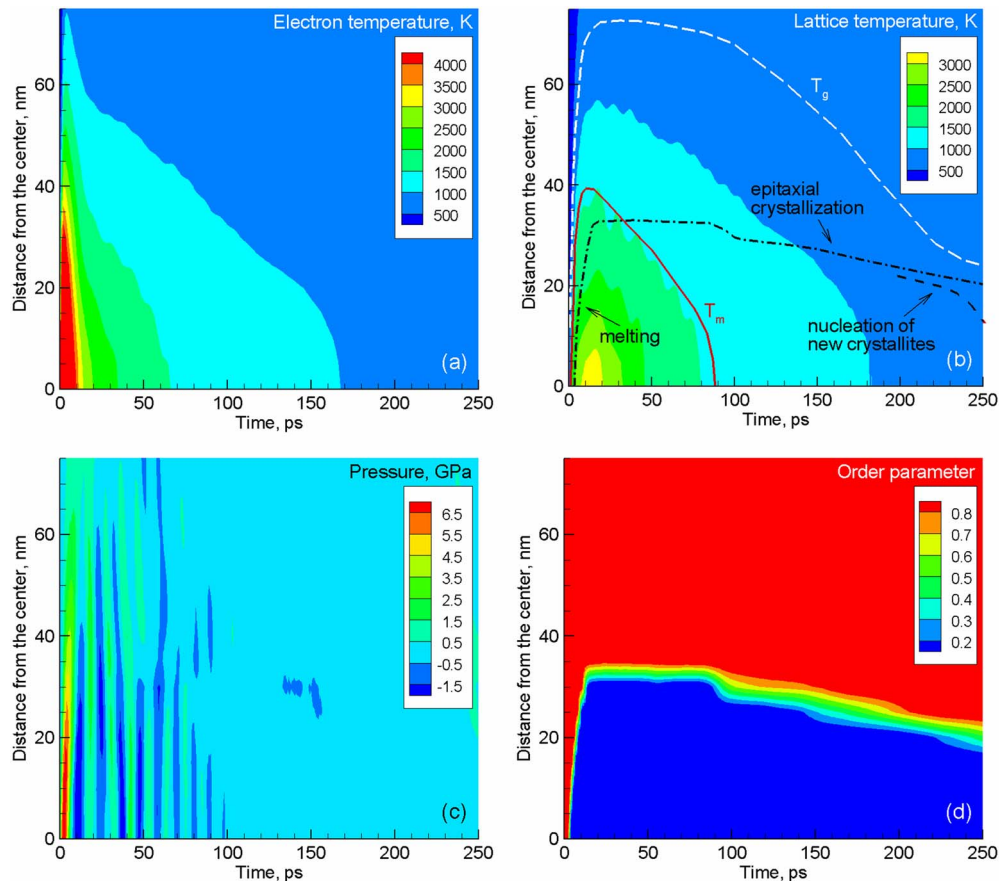


FIG. 2. (Color online) Contour plots showing the spatial and time evolution of the electron (a) and lattice (b) temperatures, pressure (c), and local order parameter (d) in a simulation illustrated in Fig. 1. The solid red and dashed white lines in (b) show the equilibrium melting temperature and glass transition temperature isotherms, respectively. The dashed-dotted black line in (b) shows the position of the liquid/crystal interface separating the liquid region from the original crystalline film, as identified from calculation of the local order parameter shown in (d). The apparent steps in the position of the solidification front at ~ 90 , ~ 145 , and ~ 225 ps in (d) are reflecting the procedure used in the data analysis and visualization rather than a real physical effect. The black dashed line in (b) corresponds to the onset of homogeneous crystallization in the undercooled liquid region, defined through the centrosymmetry parameter as the time when the number of atoms that belong to the configurations with local fcc symmetry exceeds 10% (see Fig. 5).

within a region of a Gaussian spatial profile with diameter (full width at half maximum) of 10 nm. The size of the region of the optical excitation in the simulation is similar to the characteristic size of the lateral confinement of the photoexcitation in optical near-field nanoprocesing techniques.^{16–20} The energy density deposited to the conduction band electrons within the excitation region is 3.1 J/cm^2 . In order to avoid the reflection of the laser-induced pressure wave from the radial boundary of the MD region, a special pressure-transmitting boundary condition^{27,28} is applied circumferentially around the MD part of the computational system [Fig. 1(a)].

III. RESULTS AND DISCUSSION

The visual picture of the processes triggered by the localized electronic excitation is provided by a series of snapshots of the MD part of the system shown in Fig. 1. The atoms in the snapshots are colored according to their potential energy and a sector of the film is blanked to show the distribution of the potential energy inside the film. In the initial system, the atoms located at the surface of the film have an elevated potential energy and are shown by yellow color, whereas the atoms located away from the surface have

low potential energy that corresponds to the local face-centered-cubic (fcc) surroundings and are shown by blue color. The increase in the potential energy following the laser excitation has contributions from both the thermal energy associated with the sharp temperature rise and the extra potential energy associated with melting of the central part of the film. Shortly after the laser pulse, the melted part of the film starts to move away from the substrate, leading to the formation of a hollow liquid structure (nanobump). The nanobump is stabilized by a rapid resolidification of the transiently melted region and remains as a permanent topographic feature on the surface of the irradiated film.

The conditions leading to the rapid phase transformations and generation of the frozen nanobump can be elucidated by considering the spatial and temporal evolution of the electron and lattice temperatures, pressure, and local order parameter shown for the central part of the film in Fig. 2. Laser excitation of the conduction band electrons is reflected in the sharp spike of the electron temperature [Fig. 2(a)] that reaches the maximum value of $\sim 16\,000 \text{ K}$ by the end of the laser pulse and quickly drops during the next ~ 10 ps due to the energy transfer to the lattice (electron-phonon coupling) and fast electron heat conduction in the radial directions. The energy transfer from the hot electrons to the lattice results in

the rapid increase in the lattice temperature that, by the time of 10 ps, exceeds the equilibrium melting temperature of the EAM Ni material ($T_m=1439$ K) (Ref. 24) in a central region of the film with a radius of 40 nm [Fig. 2(b)].

The overheating above the equilibrium melting temperature results in melting of the central part of the film, with the radius of the melted region reaching 33 nm by the time of 18 ps. The melting process can be clearly identified in the contour plot of the average local order parameter^{24,29} shown in Fig. 2(d). The values of the local order parameter reflect the “degree of crystallinity” of the local atomic configurations and vary from unity for a perfect fcc crystal down to values that are smaller than 0.04 for the liquid phase. The position of the liquid/crystal interface separating the melted region from the crystalline part of the film can be identified from Fig. 2(d) and is shown by the dashed-dotted line in the temperature plot [Fig. 2(b)].

The rapid heating and melting of the central part of the film during the first several picoseconds after the laser pulse take place under conditions of partial stress confinement³⁰ and result in the generation of high, up to 8 GPa, compressive stresses [red stripe in Fig. 2(c)]. The relaxation of these compressive stresses has been identified²³ to be the main driving force responsible for the acceleration of the transiently melted region of the film away from the substrate leading to the formation of the nanobump. This mechanism of the nanobump generation is different from earlier explanations proposed for the topographic surface features observed in short pulse laser nanostructuring experiments,^{13–15,31,32} where the Marangoni effect,³¹ pressure of the evaporating material,³² and plastic deformation of the irradiated film,³³ are suggested as processes being responsible for the formation of the surface nanostructures.

Analysis of the data in Figs. 2(a) and 2(b) indicates that fast two-dimensional electron heat conduction creates the conditions for a rapid cooling of the melted region, with the electron temperature dropping below the lattice temperature in the center of the melted region by 13 ps after the laser pulse. The cooling rate in the central part of the film is as high as $\sim 5 \times 10^{13}$ K/s at the beginning of the cooling process and gradually decreases down to $\sim 10^{13}$ K/s by the time of 90 ps, when the lattice temperature in the whole melted region drops below the equilibrium melting temperature [the melting temperature isotherm is shown by the solid red line in Fig. 2(b)]. The cooling rate observed in this simulation is comparable to the maximum cooling rate of about 10^{13} K/s predicted in simulations of short pulse laser interactions with a bulk Ni target at laser fluences close to the threshold for surface melting.^{4,25}

The temperature of the liquid/crystal interface drops below the equilibrium melting temperature at ~ 33 ps, starting the process of slow epitaxial resolidification. The undercooling of the liquid/crystal interface becomes deeper with time resulting in the increase in the velocity of the solidification front, which reaches the value of ~ 80 m/s by the time of 150 ps, when the temperature on the interface drops down to $0.66T_m$, and remains relatively constant while the temperature on the interface continues to decrease and reaches the value of $0.56T_m$ at 250 ps. The values of the velocity of the

solidification front observed in the simulation are comparable to the ones measured in pump-probe picosecond laser melting experiments,³⁴ where the solidification velocities are estimated to be ~ 60 and ~ 100 m/s for bulk Cu targets and thin Au films, respectively. Recent femtosecond pump-probe experiments performed for Ag films³⁵ provide information on the solidification velocities as a function of undercooling temperature. The solidification velocity is found to increase up to a maximum value of ~ 75 m/s as the temperature decreases down to $0.85T_m$ and remains approximately constant as the temperature further decreases down to $\sim 0.6T_m$. These experimental observations are consistent with the weak sensitivity of the solidification velocity to the increasing undercooling of the liquid/crystal interfacial region observed in the simulation.

The weak dependence of the solidification velocity on the degree of undercooling creates the conditions for achieving very deep undercooling in the central part of the melted region. In particular, during the time from 100 to 250 ps, the temperature in the center of the melted region decreases from $0.95T_m$ to $0.60T_m$ while the radius of the melted region shrinks from 30 to 20 nm. The velocity of the solidification front can be expected to decrease with further increase in the undercooling³⁶ but, even with a velocity of 80 m/s, it would take another 250 ps to complete the crystallization process. This raises the possibility that the melted part of the bump can be undercooled below the glass transition temperature, leading to a transient formation of a one-component metallic glass. To test the possibility of this scenario, we calculate the glass transition temperature of the EAM Ni material, T_g . The glass transition temperature is determined from the temperature dependence of the shape of the pair distribution function (PDF) calculated in a separate set of MD simulations. The simulations are performed for a system of 4000 atoms, with periodic boundary conditions applied in all directions. The initial system is melted and equilibrated at a temperature above the melting point. The atomic configurations used in the calculations of PDFs are obtained by fast cooling of the liquid structure to the desired temperature, followed by equilibration for 50 ps at zero pressure and constant temperature. After the equilibration, the data for PDF is collected every 0.5 ps during the following 50 ps, and the final PDF is obtained by averaging over the 100 instantaneous data sets. The PDFs calculated at different temperatures, from 300 to 2000 K, are shown in Fig. 3(a). The transition from the undercooled liquid to the amorphous state is manifested by the characteristic splitting³⁷ of the second peak of PDF below 600 K. Following the empirical criterion suggested in Ref. 38, the glass transition temperature is found from the temperature dependence of the ratio of the magnitudes of the first minimum to the first maximum of PDFs $R=g_{\min}/g_{\max}$ shown in Fig. 3(b). The value of $T_g=717$ K= $0.5T_m$ is determined from the point of intersection of the linear extrapolations of the liquid and amorphous branches of the $R(T)$ dependence. The deviations of R from the linear trends at and around 700 K are related to the onset of the crystallization process during the 100 ps of the MD simulations used for equilibration of the system and calculation of PDFs.

An isotherm corresponding to the glass transition tem-

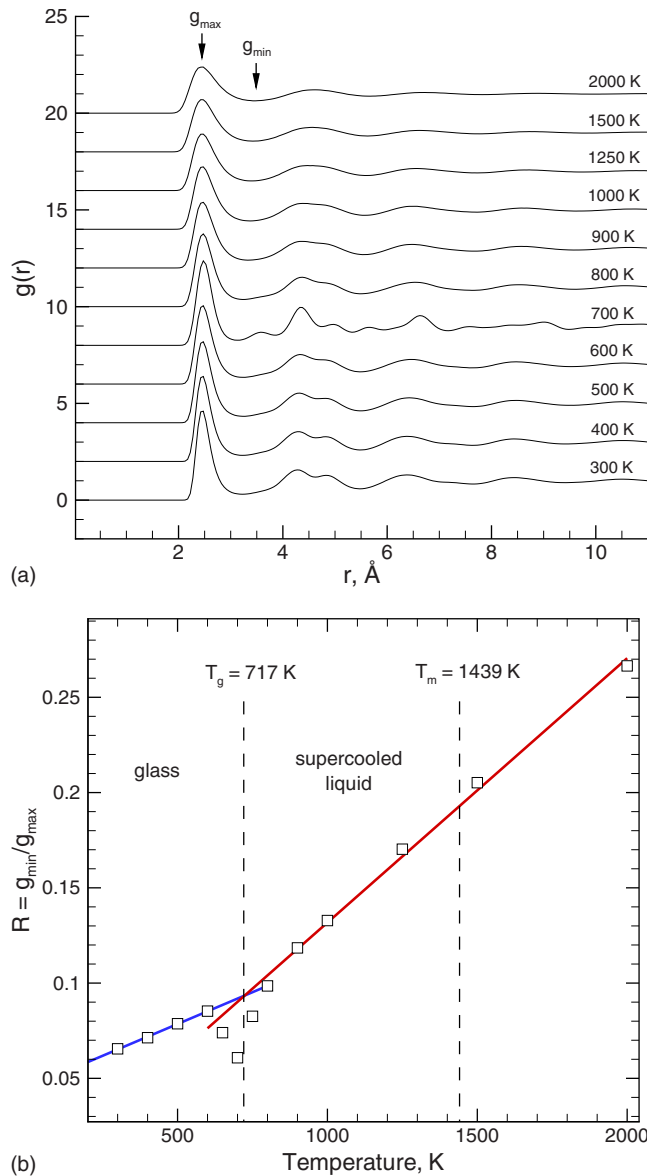


FIG. 3. (Color online) PDF calculated for EAM Ni at different temperatures (a) and the ratio of the magnitudes of the first minimum to the first maximum of the PDFs, $R = g_{\min}/g_{\max}$, used for identification of the glass transition temperature (b).

perature of EAM Ni is shown by the white dashed line in Fig. 2(b). The slope of the isotherm in Fig. 2(b) is substantially higher than the slope of the line showing the advancement of the liquid/crystal interface and, by the time of 225 ps, the isotherm gets within just 5 nm from the liquid region. In the last 25 ps of the simulation, however, the slope of the isotherm decreases and the isotherm becomes almost parallel to the line showing the advancement of the solidification front. This change in the slope of the isotherm can only partially be attributed to the gradual decrease in the temperature gradients with time. An additional important factor that slows down the cooling process, and even results in a localized reheating of parts of the melted region, is the onset of a massive homogeneous nucleation of crystallites throughout the deeply undercooled liquid region.

A visual picture of the nucleation and growth of the crystalline regions is provided in Fig. 4, where snapshots of the

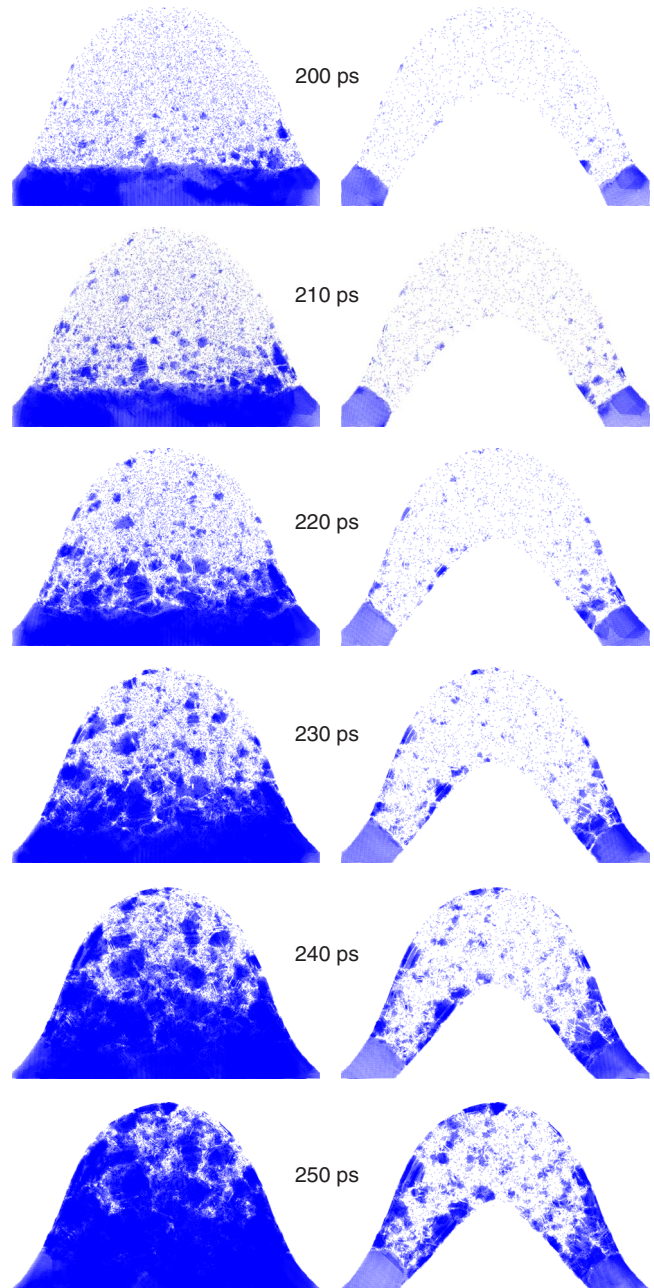


FIG. 4. (Color online) Snapshots of the central region (nanobump) of the irradiated film illustrating the crystallization process during the final 50 ps of the simulation. All atoms that do not belong to the configurations with local fcc symmetry ($CSP > 1$) are blanked. All fcc atoms are shown in the left frames, whereas, only 7 nm slices cut through the center of the MD domain are shown in the right frames. The configurations are quenched using the velocity damping technique for 2 ps prior to the structural analysis to reduce thermal noise in atomic positions.

central region of the irradiated film are shown for the final 50 ps of the simulation. Only atoms that belong to the crystalline parts of the system are shown in the snapshots, with the distinction between the crystalline and liquid regions done based on the values of the centrosymmetry parameter (CSP) (Ref. 39) calculated for all atoms. Unlike the local order parameter used in the analysis of the melting and epitaxial recrystallization processes [Fig. 2(d)], CSP is not sensitive to the rotation of an atomic structure and can be used for identification of randomly oriented crystallites. In order to reduce

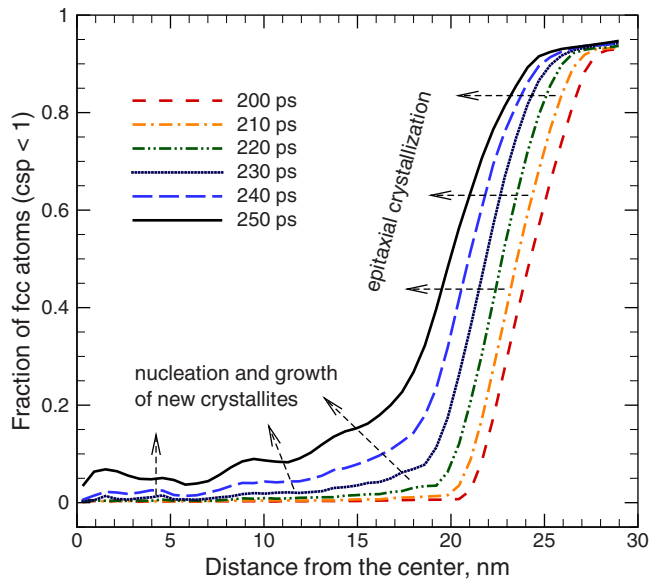


FIG. 5. (Color online) The fraction of atoms with local fcc structure (CSP < 1) in the central region (nanobump) of the irradiated film. The arrows schematically show the contributions of the epitaxial regrowth of the original crystalline film and nucleation of new crystallites inside the undercooled liquid.

the thermal noise in atomic positions, the structural analysis is preceded by quenching the atomic configurations for 2 ps using a velocity dampening technique, where the velocity of each individual atom is set to zero each time when the kinetic energy of the atom is maximized. The fast quenching does not introduce any structural changes to the atomic configurations but makes the visualization and structural analysis more straightforward. The homogeneous nucleation starts at ~ 200 ps when the temperature of the liquid near the liquid/crystal interface drops below $0.6T_m$. The density of the crystal nuclei is higher at the periphery of the liquid region, where the undercooling is larger, although the nucleation process quickly extends to the whole liquid region.

The onset of the contribution of the homogeneous nucleation to the crystallization process can be clearly seen from the spatial distributions of the fraction of atoms with local crystalline surroundings shown in Fig. 5. Until ~ 200 ps, the increase in the fraction of atoms in the crystal phase is limited to the region of the liquid/crystal interface and corresponds to the propagation of the solidification front. At a later time, however, the atomic configurations with crystalline structure start to appear ahead of the solidification front, reflecting the contribution of the homogeneous nucleation and growth of new crystallites. The relatively small fraction of fcc atoms observed in the central part of the system at the end of the simulation ($< 10\%$) is defined not only by the fact that the crystallization process is not completed by this time, but also by the procedure used to identify the “fcc atoms” as atoms with local fcc surroundings, which excludes a large number of atoms located at the surfaces of the growing crystallites. From the snapshot of the atomic configuration of the nanobump taken at the end of the simulation (Fig. 6), in which all but the surface atoms are shown, one can see that the homogeneous crystallization has resulted in the formation of a complete layer with nanocrystalline structure in the

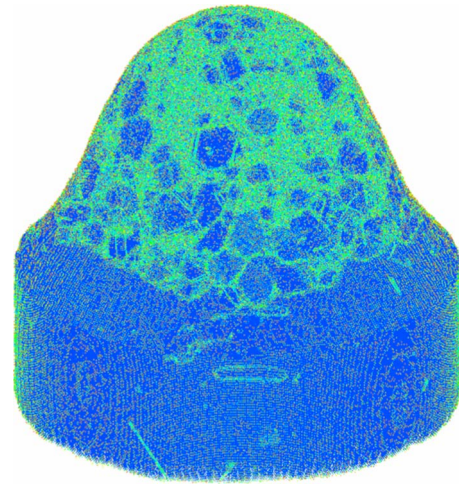


FIG. 6. (Color online) Snapshot of the central region (nanobump) of the irradiated film taken at 250 ps after the laser pulse. The atoms are colored according to their CSP. Atoms that belong to the configurations with local fcc symmetry are colored blue, atoms that belong to the undercooled liquid and crystal defects (grain boundaries, dislocations, and point defects) are colored green. Surface atoms (CSP > 20) are blanked in the image. The configurations are quenched using the velocity dampening technique for 2 ps prior to the structural analysis to reduce thermal noise in atomic positions.

vicinity of the epitaxial solidification front, whereas at the top of the nanobump individual crystallites are still surrounded by the undercooled liquid. The solidification process is likely to be completed within the next 50–100 ps, leading to the formation of the nanocrystalline structure of the nanobump.

IV. CONCLUSION

The localized laser energy deposition in a metal film creates the conditions for a sequence of rapid phase transformations occurring under highly nonequilibrium conditions. The fast energy transfer from the excited electrons to the lattice results in a strong overheating and rapid homogeneous melting^{24,40} of a nanoscale region of the irradiated film. The melting is immediately followed by cooling and resolidification of the transiently melted region. Due to the small size of the melted region, steep temperature gradients, and fast two-dimensional electron heat conduction, the cooling rate is extremely high and exceeds 10^{13} K/s at the initial stage of the cooling process. As a result, the resolidification proceeds under conditions of increasingly deep undercooling below the equilibrium melting temperature. The velocity of the propagation of the liquid/crystal interface quickly rises up to its maximum value of ~ 80 m/s and stays approximately constant as the temperature of the melted region continues to decrease. When the temperature reaches the level of $\sim 0.6T_m$, a massive homogeneous nucleation of crystallites inside the undercooled liquid region starts and prevents further undercooling of the liquid down to the glass transition temperature of $0.5T_m$. Note that the ability to achieve the glass transition temperature without the onset of the homogeneous solidification would imply only a temporal transition to the amorphous state, which is unlikely to be stable in the presence of crystalline regions. Indeed, it has been predicted in recent

MD simulations that the solidification velocity in one-component metals remains finite even significantly below the glass transition temperature.^{35,41}

The results of the simulation, therefore, predict the formation of a nanocrystalline structure in the regions of the irradiated target experiencing localized melting and resolidification. The nanocrystalline materials have a number of attractive characteristics, such as high hardness and strength,^{42,43} and the prediction of the nanocrystalline structure of surface features generated in laser processing of metal surfaces can have important implications for practical applications. To our knowledge, there have been no experimental studies aimed at microstructural analysis of surface structures generated by localized photoexcitations of metal targets^{13–22,31,32} and the computational predictions reported in this paper still await experimental verification.

ACKNOWLEDGMENTS

The work is supported by the National Science Foundation (USA) through Grant Nos. CBET-0348503 and DMR-0907247, an EU Marie-Curie Transfer of Knowledge Award No. MTKD-CT-2004-509825 to the National University of Ireland, Galway, the Deutsche Forschungsgemeinschaft through the Emmy Noether program under Grant No. RE 1141/11, and the NSF sponsored Renewable Energy Materials Research Science and Engineering Center (REMSEC) at the Colorado School of Mines.

¹D. Turnbull and R. E. Cech, *J. Appl. Phys.* **21**, 804 (1950).

²D. M. Herlach, *Mater. Sci. Eng. R.* **12**, 177 (1994).

³C.-J. Lin, F. Spaepen, and D. Turnbull, *J. Non-Cryst. Solids* **61–62**, 767 (1984).

⁴W. H. Duff and L. V. Zhigilei, *J. Phys.: Conf. Ser.* **59**, 413 (2007).

⁵W. A. Elliott, F. P. Gagliano, and G. Krauss, *Appl. Phys. Lett.* **21**, 23 (1972).

⁶C. J. Lin and F. Spaepen, *Acta Metall.* **34**, 1367 (1986).

⁷J. A. Alonso and J. M. Lopez, *Mater. Lett.* **4**, 316 (1986).

⁸D. Turnbull, *Contemp. Phys.* **10**, 473 (1969).

⁹M. H. Bhat, V. Molinero, E. Soignard, V. C. Solomon, S. Sastry, J. L. Yarger, and C. A. Angell, *Nature (London)* **448**, 787 (2007).

¹⁰Y. Hirayama and M. Obara, *J. Appl. Phys.* **97**, 064903 (2005).

¹¹Y. Hirayama and M. Obara, *Appl. Surf. Sci.* **197–198**, 741 (2002).

¹²P. P. Pronko, S. K. Dutta, J. Squier, J. V. Rudd, D. Du, and G. Mourou, *Opt. Commun.* **114**, 106 (1995).

¹³F. Korte, J. Koch, J. Serbin, A. Ovsianikov, and B. N. Chichkov, *IEEE Trans. Nanotechnol.* **3**, 468 (2004).

¹⁴J. Koch, F. Korte, T. Bauer, C. Fallnich, A. Ostendorf, and B. N. Chich-

kov, *Appl. Phys. A: Mater. Sci. Process.* **81**, 325 (2005).

¹⁵A. I. Kuznetsov, J. Koch, and B. N. Chichkov, *Appl. Phys. A: Mater. Sci. Process.* **94**, 221 (2009).

¹⁶J. Jersch, F. Demming, J. Hildenhausen, and K. Dickmann, *Opt. Laser Technol.* **29**, 433 (1997).

¹⁷J. Jersch, F. Demming, L. J. Hildenhausen, and K. Dickmann, *Appl. Phys. A: Mater. Sci. Process.* **66**, 29 (1998).

¹⁸A. Chimmalgi, T. Y. Choi, C. P. Grigoropoulos, and K. Komvopoulos, *Appl. Phys. Lett.* **82**, 1146 (2003).

¹⁹C. P. Grigoropoulos, D. J. Hwang, and A. Chimmalgi, *MRS Bull.* **32**, 16 (2007).

²⁰D. Hwang, S.-G. Ryu, N. Misra, H. Jeon, and C. P. Grigoropoulos, *Appl. Phys. A: Mater. Sci. Process.* **96**, 289 (2009).

²¹S. M. Huang, M. H. Hong, B. Lukiyanchuk, and T. C. Chong, *Appl. Phys. A: Mater. Sci. Process.* **77**, 293 (2003).

²²Y. Lu and S. C. Chen, *Nanotechnology* **14**, 505 (2003).

²³D. S. Ivanov, B. Rethfeld, G. M. O'Connor, Th. J. Glynn, A. N. Volkov, and L. V. Zhigilei, *Appl. Phys. A: Mater. Sci. Process.* **92**, 791 (2008).

²⁴D. S. Ivanov and L. V. Zhigilei, *Phys. Rev. B* **68**, 064114 (2003).

²⁵L. V. Zhigilei, Z. Lin, and D. S. Ivanov, *J. Phys. Chem. C* **113**, 11892 (2009).

²⁶X. W. Zhou, H. N. G. Wadley, R. A. Johnson, D. J. Larson, N. Tabat, A. Cerezo, A. K. Petford-Long, G. D. W. Smith, P. H. Clifton, R. L. Martens, and T. F. Kelly, *Acta Mater.* **49**, 4005 (2001).

²⁷L. V. Zhigilei and B. J. Garrison, *Mater. Res. Soc. Symp. Proc.* **538**, 491 (1999).

²⁸C. Schäfer, H. M. Urbassek, L. V. Zhigilei, and B. J. Garrison, *Comput. Mater. Sci.* **24**, 421 (2002).

²⁹J. R. Morris and X. Song, *J. Chem. Phys.* **116**, 9352 (2002).

³⁰E. Leveugle, D. S. Ivanov, and L. V. Zhigilei, *Appl. Phys. A: Mater. Sci. Process.* **79**, 1643 (2004).

³¹F. Korte, J. Koch, and B. N. Chichkov, *Appl. Phys. A: Mater. Sci. Process.* **79**, 879 (2004).

³²Y. Nakata, T. Okada, and M. Maeda, *Jpn. J. Appl. Phys., Part 2* **42**, L1452 (2003).

³³Y. P. Meshcheryakov and N. M. Bulgakova, *Appl. Phys. A: Mater. Sci. Process.* **82**, 363 (2006).

³⁴C. A. MacDonald, A. M. Malvezzi, and F. Spaepen, *J. Appl. Phys.* **65**, 129 (1989).

³⁵W. L. Chan, R. S. Averback, D. G. Cahill, and Y. Ashkenazy, *Phys. Rev. Lett.* **102**, 095701 (2009).

³⁶K. A. Jackson, *Interface Sci.* **10**, 159 (2002).

³⁷G. S. Cargill III, in *Solid State Physics*, Structure of Metallic Alloy Glasses, edited by H. Ehrenreich, F. Seitz, and D. Turnbull (Academic Press, New York, 1975), Vol. 30, pp. 227–320.

³⁸H. R. Wendt and F. F. Abraham, *Phys. Rev. Lett.* **41**, 1244 (1978).

³⁹C. Kelchner, S. J. Plimpton, and J. C. Hamilton, *Phys. Rev. B* **58**, 11085 (1998).

⁴⁰B. Rethfeld, K. Sokolowski-Tinten, D. von der Linde, and S. I. Anisimov, *Phys. Rev. B* **65**, 092103 (2002).

⁴¹Y. Ashkenazy and R. S. Averback, *EPL* **79**, 26005 (2007).

⁴²H. Gleiter, *Acta Mater.* **48**, 1 (2000).

⁴³K. S. Kumar, H. Van Swygenhoven, and S. Suresh, *Acta Mater.* **51**, 5743 (2003).